Advanced Robotics, Vol. 16, No. 3, pp. 233–250 (2002)

Full paper

Development of a high-performance direct-drive joint

FARHAD AGHILI[1,*], MARTIN BUEHLER[2] and JOHN M. HOLLERBACH[3]

[1] *Canadian Space Agency, Space Technologies, Spacecraft Engineering, Saint-Hubert, Quebec J3Y 8Y9, Canada*
[2] *Department of Mechanical Engineering, McGill University, Montreal, Quebec H3A 2A7, Canada*
[3] *School of Computing, University of Utah, Salt Lake City, UT 84112, USA*

Received 29 January 2001; accepted 28 September 2001

Abstract—This paper reports on advances in the design and development of a high-performance direct-drive joint for robotics and automation. The joint integrates a motor, a torque sensor and joint bearings. The key design aspects of the motor, such as the armature, motor housing, bearing arrangement and sensors, are detailed. The description of a dynamometer testbed with a hydraulic active load used for motor calibration and to test the dynamic behavior of the motor and its entire control system is also given. We also present a number of advanced implementations in control, motor torque control and motion control using positive joint torque feedback. Experimental results illustrate outstanding performance regarding thermal response, torque ripple, reference trajectory tracking, torque disturbance rejection and joint stiffness.

Keywords: Direct drive motor; robot joint; actuator; motion control; mechatronics.

1. INTRODUCTION

Today's joint servos for motion control must meet stringent demands for speed and accuracy. In particular, industrial robots for laser cutting, arc welding, fixture-less assembly, flexible manufacturing and indexing require precise and high bandwidth tracking accuracy as well as good disturbance rejection properties. Conventional electric motors with their high speed and low torque are not ideal for these tasks, since they require gears which degrade performance due to backlash, stiction, friction and compliance. Internal friction in gears introduces motor torque losses of 10–50%. Moreover, a gear ratio n multiplies the motor's rotor inertia seen by the load by n^2 which further reduces the maneuverability and bandwidth of geared robots [1].

These disadvantages are avoided or reduced with direct-drive actuators, which can produce the torque–speed characteristics required in many high performance

*To whom correspondence should be addressed. E-mail: farhad.aghili@space.gcca

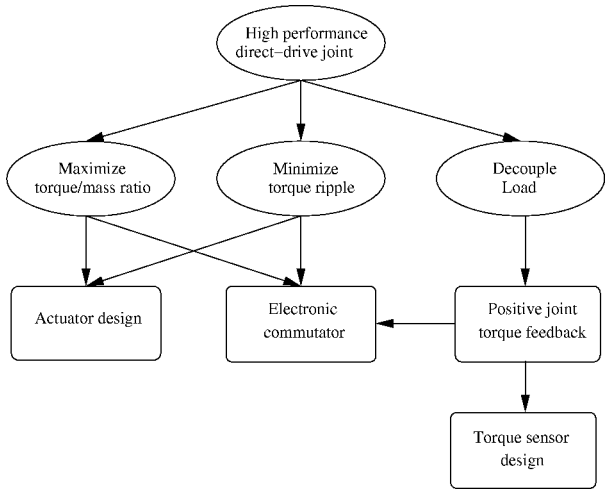

Figure 1. Design goals.

motion control tasks without additional gearing [1, 2]. The main advantages claimed for direct-drive robots are high accuracy and speed, light weight, high stiffness, and mechanical design simplicity. However, direct-drive systems are more sensitive to the actuator's torque ripple and they also suffer from lower continuous torque compared to geared motors. Moreover, they are sensitive to load torques due to the lack of the attenuation effect of a gearbox. In light of these shortcomings, we pursued a multi-objective agenda towards improving direct-drive joint performance as depicted in Fig. 1. For instance, torque-to-mass ratio can be improved either by reducing the motor's thermal resistance through special design of the motor's armature [3–5] or by minimizing power losses through optimal commutation [6, 7]. The motor torque ripple can be reduced either by improving motor design such as skewing and fractional slot pitch windings [8] or by implementing a proper torque control. The sensitivity of the direct-drive joint to load torque can be suppressed via positive joint torque feedback [9–11] if it is possible to integrate a suitable torque sensor [12].

Recently, axial-airgap synchronous motors were identified to be superior for direct-drive actuation [3, 4] and several prototypes of such a motor, the 'McGill/MIT' [3] motor, in single axial air-gap configurations have been constructed. The key design feature — a 'pancake' shape armature with *water cooling* — increases the allowable continuous current and therefore the torque-to-mass ratio. This paper describes the design and control system of the fourth iteration of the McGill/MIT motor, and the components of the complete direct-drive system and the experimental tools necessary for its calibration, control and performance test (Fig. 2). A number of advanced implementations on this motor have been presented in the past which address the minimization of torque ripple [6, 7] and motion control using positive joint torque feedback [9, 10].

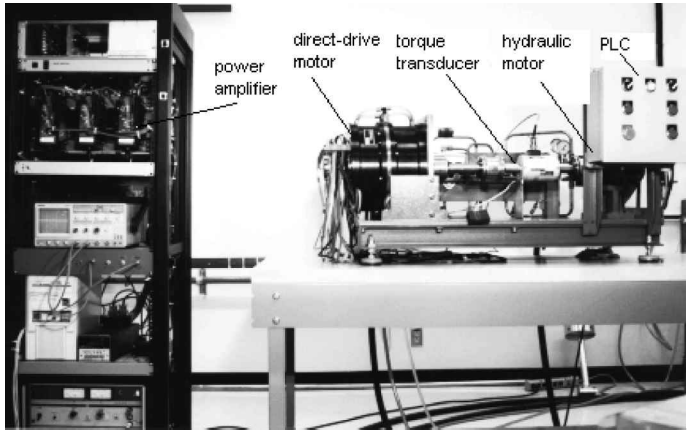

Figure 2. The experimental set-up.

This paper is organized as follows. Section 2 describes the design of the direct-drive joint along with the system components and the related experimental hardware which will be used subsequently. The main objective of the section encompasses the armature design, while engineering issues in the design of the motor, specifically the motor's housing and bearing configuration, will also be discussed. The thermal aspect of the motor is also characterized experimentally. The motor is equipped with a specifically designed torque sensor which is described in Section 3. The mechanical structure and geometry of this sensor is carefully designed to be suitable for joint torque measurement, and its prominent mechanical features are proven experimentally. Section 4 describes the control system which is composed of torque control and motion control utilizing positive joint torque feedback. The foci are on implementation aspects of the controller and the performance test results, while control design details are available in the cited references. Finally, the description of a dynamometer testbed with a hydraulic active load is given in Section 5. The system is used to calibrate the motor, and to test the dynamic behavior of the motor and its entire control system.

2. MOTOR DESIGN

2.1. General description

The structure of the actuator is adopted from the McGill/MIT motor whose design goal is to solve the main problems with direct-drive electric motors: large size and weight of theses motors relative to their torque and torque ripple production [3]. Specific goals in the design of McGill/MIT motor have been:

- Torque-to-mass ratio 10 Nm/kg.
- A torque accuracy of 1%.

The McGill/MIT motor is a three-phase synchronous device with an axial air gap which optimizes the torque-to-mass ratio [3]. The axial air gap, however, introduces an extensive attractive force between the armatures which creates a reaction force on the motor's bearings. The major development in the new design is using double armature pairs to cancel out the reaction force. The bearing arrangement is carefully designed to minimize friction and weight as well as to maximize stiffness. Water cooling of the armatures is another feature of the design which improves the capability of the system to remove heat. Significant improvements have been made in the underlying design listed as follows:

- A complete joint structure, with dual armatures for balanced axial loading and integral water cooling system.
- Housing and bearing arrangment suitable for a robot joint.
- Integrated torque sensor for direct measurement of joint torque.

In addition to the mechanical design improvemnts, control strategies of this motor have been successfully implemented that are documented in [6, 7, 9].

2.2. Armature

Most electric motors deliver their maximum power at high velocity. The number of poles in motors plays the role of the gear ratio in gears which typically reduces velocity and increases torque. However, increasing the number of poles has several practical limitations. Multi-pole motors require complex designs with many slots and windings, increasing cost. In addition, they require high-frequency control signals which can be challening for electronic commutators [6]. Therefore, the number of poles and slots should be determined by a trade-off between manufacturing capability and controllability. Figure 3 shows the armature prototype with three phases wound over six slots per pole to create 18 poles. The resulting 108 slots are skewed by a full slot pitch to minimize torque ripple. The armature core is machined out of a ring rolled from a sheet of standard transformer iron that minimizes core losses. Glue treatment is performed between sheets during the

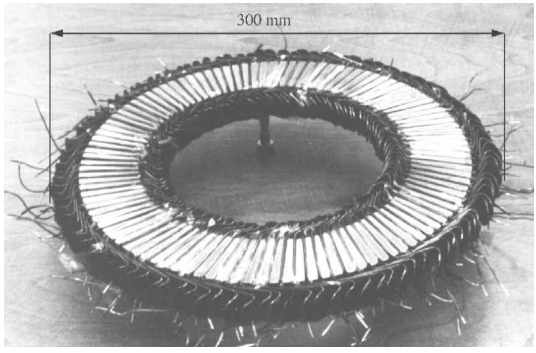

Figure 3. The prototype armature with 108 skewed slots.

lamination to solidify the laminated core. Although core losses tend to increase with sheet thickness, very thin sheets are not efficient because of high occupancy ratio of isolation layer and of the glue. We chose 0.5 mm thick strip to make the laminated core with inside and outside diameters of 180 and 260 mm. In order to maximize the packing factor, the armature coil is made of square wire (28 gage).

The maximum motor torque is determined by the maximum allowable current subjected to magnetic saturation. Magnetic saturation is a material-dependent property, while the maximum winding current depends on the thermal characteristics of a motor. Since magnetic saturation occurs almost instantaneously and the thermal time constant is relatively large, the magnetic saturation and thermal saturation dictate the motor's instantaneous and continuous torque capability, respectively. Since, typically, the continuous torque is the lower limit, it is aimed to be maximized in our motor prototype. In the case of wound-field motors, the maximum attainable continuous torque, $\tau_{\max}$, is proportional to the square of the maximum admissible current, i^2, which is in turn proportional to the maximum power loss, P_{loss}. On the other hand, the maximum allowable power losses times the thermal resistance:

$$R_{\text{th}} = \frac{\Delta T}{P_{\text{loss}}}, \tag{1}$$

gives the maximum allowable temperature rise, ΔT. Therefore, it can be concluded that:

$$\tau_{\max} \propto 1/R_{\text{th}}, \tag{2}$$

which implies that the maximum torque is inversely proportional to the capability of the motor to remove heat, requiring a low thermal resistance. Most motors dissipate heat by convection and radiation. This is not very effective. Much better cooling can be achieved by water circulation, which increases the torque-to-mass ratio. It is imperative to bring the water circulation in proximity to the heat-producing copper windings. To this end, several copper tubes are placed close to the windings and the armatures were potted in thermally conductive epoxy (Emerson and Cumming Stycast 2850FT).

The thermal step responses of the motor prototype to different amplitude three-phase currents are shown in Fig. 4(left). The solid and dashed curves correspond to the system response with and without water circulation. The exponential temperature curves resemble the response of a first-order system. It is quite clear that the system time constant decreases considerably by water circulation and so does the asymptotic temperature. Figure 4(right) illustrates the steady-state temperature versus power losses. The slope of the lines approximates the thermal resistances of the windings to the ambient air with and without water cooling are 0.42 and 0.07°C/W, respectively. Thus, by virtue of (2), one can conclude that the water cooling improves the continuous torque capability by a factor of 6.

Another key feature of a direct-drive joint is limited joint rotation and hence limited motor rotation. The maximum motor excursion can be expected to be

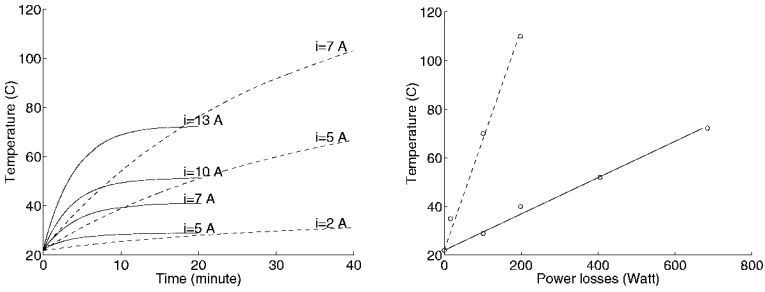

Figure 4. Armature temperature step response (left), and steady-state temperature versus power losses (right) with water cooling (solid line) and without water cooling (dashed line).

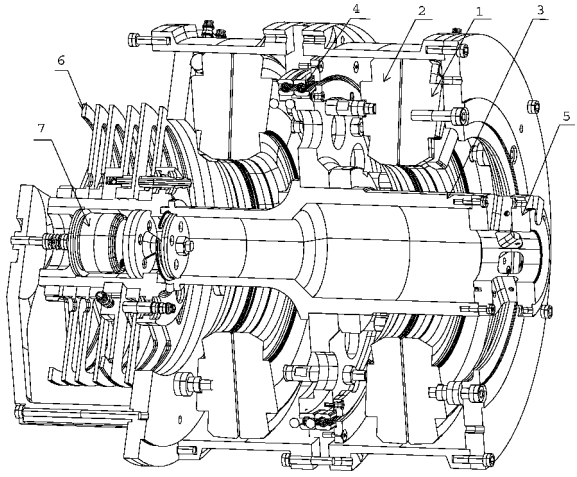

Figure 5. Cross section of the direct-drive motor. 1, Stator armature; 2, rotor armature; 3, hollow shaft; 4, bearing; 5, torque sensor; 6, wire and tube separator; 7, encoder.

limited to 360°. Since the motor is not required to rotate more than 360°, connection for water cooling across the air gap as well as electrical connection to the rotor are made without slip rings. The cable routing and the tube routing are separated by an array of aluminum disks (Fig. 5).

2.3. Motor housing

The motor housing contributes nothing to torque production, but can significantly decrease the motor's torque-to-mass ratio. Therefore, it is vital to minimize its weight while maintaining its strength. The housing elasticity permits the magnetic forces to reduce the air gap, which, in turn, increases the magnetic forces. As a consequence, the air gap can collapse. The subsequent analysis will determine the minimum stiffness for a *stable air gap.*

The magnetic energy in the air gap is $-c/x$, where x is the distance between the two armatures and c is a constant [13]. Suppose the elasticity of the housing is represented by its axial stiffness k_h. Now the total magnetic and elastic potential

energy, $E(x)$, is:

$$E(x) = -\frac{c}{x} + \frac{1}{2}k_h(x - x_0)^2,$$

where x_0 is the air gap distance in the absence of any deflection force. Let $x = \delta$ be the equilibrium point which is the solution of $dE(x)/dx = 0$. Then the necessary condition for a locally stable equilibrium is $d^2E(x)/dx^2 > 0$ at $x = \delta$. Hence:

$$\left.\frac{d^2E(x)}{dx^2}\right|_{x=\delta} = -\frac{2c}{\delta^3} + k_h > 0.$$

Since the magnetic force is $f = c/\delta^2$, the condition for a stable airgap is $k_h > 2f/\delta$. The structural stiffness of the housing must be higher than the *critical stiffness* $2F/\delta$. For our motor, the maximum axial force is calculated as $f = 32$ kN while the nominal airgap is 1.3 mm [13], which specifies the critical stiffness to be 5×10^7 N/m. To be on the safe side, the motor housing is designed such that the equivalent stiffness of the armature and housing is twice this critical value.

2.4. Bearing arrangement

Precision of a robot cannot be achieved even with a sophisticated controller if the mechanical parts of the system fail to operate precisely. In a direct-drive joint, the motor bearing set, which supports both rotor and robot arm, is the only moving part and hence the main source of mechanical imperfections. These can be caused by dry friction, tolerances or deflection. Therefore, the bearings must be chosen carefully in a suitable arrangement.

According to International Standard ISO 9283, two important robot performance criteria are path repeatability and distance repeatability. These are determined by how much of the hysteresis of each joint is caused by friction and the cumulative effect of bearing tolerances. The other relevant specification is static compliance, i.e. the maximum displacement of a robot's tip per unit of applied load on the robot's tip. Depending on the applications, the applied load can be any components of the generalized forces/moments. The tip displacement is determined by the combination of the joint controller, robot links and bearing compliances. Since the robot control is usually based on joint angle sensing, the bearing deflection cannot be compensated by control. Hence, joint stiffness is another design consideration which adversely affects the positioning accuracy. The other design issue is that the bearing should be able to carry the required load while contributing only minimum weight.

Axial air gaps produce huge attraction forces, estimated to be up to 32 kN for our motor prototype, which can adversely affect friction and lifetime of the bearings. The major development in the new design is the use of double armature pairs to cancel out the reaction force [3]. To achieve this, we integrate two motors back-to-back such that the axial forces are taken by the motor's aluminum housing, as shown in Fig. 5. The armatures in the middle (rotors) are the rotating parts which

are mounted to the motor's shaft while the two other armatures (stators) are mounted to the motor's housing. Each stator–rotor armature pair is a complete motor which can be assembled separately. This facilitates motor assembly and airgap adjustment. Moreover, an evaluation of several bearing configurations revealed that a centered bearing placement (Fig. 5) is superior. Since the rotors are pivoted at the middle, the variation of both air gaps due to elastic deflection of the housing are altered equally and the axial forces remain identical.

The next design step is selecting bearing type and size. Generally, the reaction forces on the bearings are due to external shear and axial forces, but primarily bending moments. Therefore the bearing has to have desirable bending properties. Generally, bearing stiffness is determined by the type, size and number of its balls or rollers. The heavier bearings are usually the stiffer ones; however, this is not desirable, specially for direct-drive robots. A thin-section bearing has a greater number of balls than a conventional bearing, which yields higher stiffness and load carrying capability compared to a same weight conventional bearing [14]. Moreover, large-diameter bearings have high bending stiffness as the reaction forces on the rolling elements decrease with increasing diameter for a given moment. On the other hand, the tolerances do not increase as much with the diameter [14]. This is important for endpoint positioning accuracy because the robot control is usually based on joint angle sensing that cannot compensate the bearing deflection. The friction torque at the bearing tends to increase with an increase in bearing bore diameter and radial load. Yet, since the reaction bearing force due to external bending moment decreases with larger diameter, the friction does not depend on the size of bearing. In short, thin-section bearings save both space and weight and a larger bearing diameter is desirable, of course within the limitation of cost and geometrical feasibility.

Finally, a pair of *thin-section angular contact ball bearings* (Kaydon KD100ARO) of 254 mm inside diameter was chosen. The bearings are mounted back-to-back to achieve high stiffness (2.5×10^7 Nm/rad) and they come with pre-specified medium duty payload. Without a gearbox, the bearing friction is the only source of joint friction. [Figure 10A shows joint friction that is measured by rotating the motor shaft in a quasi-static manner by using the hydraulic dynamometer described in Section 5.] It is evident that the friction is fairly low at ± 1 Nm and position independent.

Figure 6 illustrates the motor prototype whose external dimensions are 260 mm in length and 320 mm in diameter.

3. SENSORS

The motor is instrumented with sensors for winding temperature, joint angle and joint torque. To monitor the thermodynamic behavior of the motor, six *thermocouples* (Omega JMTSS-02OU-6) are placed in the vicinity of each winding phase of the rotor and stator. The thermocouples are accompanied by signal conditioning (National Instrument NI 776289-J) which perform cold-junction compensation.

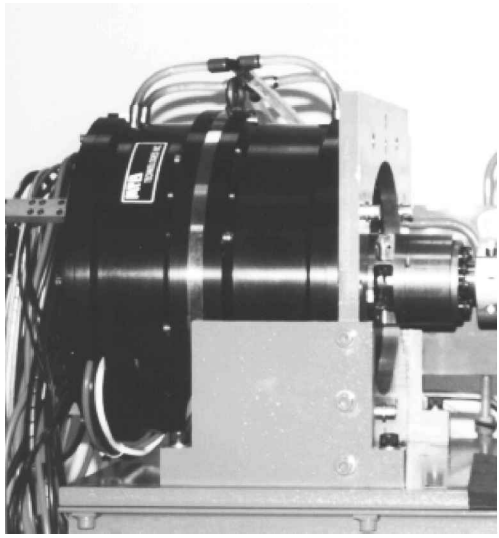

Figure 6. The motor prototype.

Position sensing is required to perform both electronic commutation and motion control. Since the commutation needs absolute position measurement, resolvers seem to be adequate. However, their limited resolution poses difficulties for achieving low torque ripple [15] and precise control. Instead, an optical encoder (Teledyne Gurley 8321-4500-CBQA-NB) is mounted to the motor shaft while the encoder shaft is fixed to the motor's housing by a small bellow-type coupling (Fig. 5). The resolution of the encoder is multiplied 80 times by an interpolator for 0.001° final resolution.

Joint torque feedback plays an important role in suppressing the effect of load torque on the motion servo. However, accurate joint torque sensing is difficult, especially in robotic applications, due to large non-torsional force/moments. Moreover, in order to increase the signal-to-noise ratio and obtain a high resolution, it is desirable to design an elastic structure which generates a large strain for torsion but exhibit low strain sensitivity to bending. Figure 7 shows a novel torque sensor designed and integrated with this motor [12, 16]. The sensor output versus torque is plotted in Figure 8(left). The maximum deviation from non-linearity is 0.2% full scale. Figure 8(right) shows the frequency response of the sensor flanged to a massive steel disk, revealing two distinct modal frequencies which belong to torsion and bending modes. The corresponding torsion and bending stiffnesses are 2.4×10^5 and 4.8×10^6 Nm/rad, respectively. Moreover, with a measured cross sensitivity of 0.6% the sensor can tolerate extensive non-torsional force/moment components.

Experiments on the previous motor prototype showed that the integrated sensors, i.e. encoder and torque sensor, are likely to be adversely affected by armature heat or strong magnetic field. This problem is solved in the new design by enclosing the

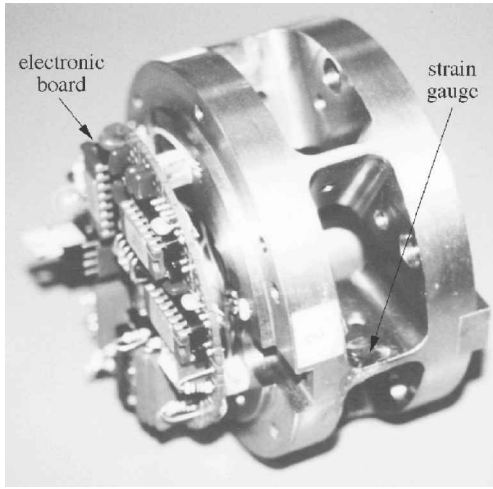

Figure 7. The torque sensor prototype.

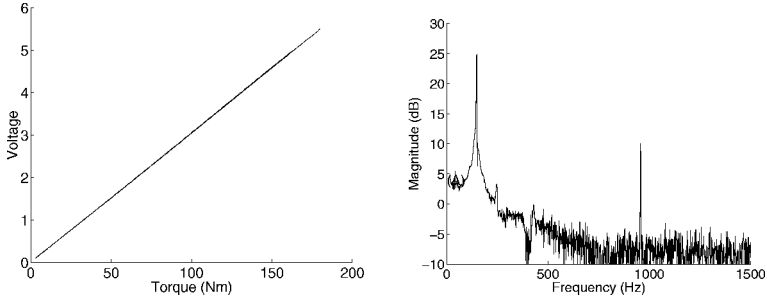

Figure 8. Sensor output versus applied torque (left) and frequency response of the sensor system (right).

sensors in the hollow shaft (Fig. 5) which protects the sensors by providing thermal and magnetic insolation.

4. CONTROL

Figure 9 illustrates the block diagram of the control system which consists of three complementary subsystems: ripple-free torque control, positive joint torque feedback to decouple load torque and PID motion control.

4.1. Torque control and power electronics

The torque control subsystem comprises an electronic commutator and current amplifiers, critical elements for the overall system performance. The torque control problem, also known as the commutation law, is how to modulate the current phases i_j $(j = 1, 2, 3)$ as a function of position θ, such that the desired set-point torque τ^*

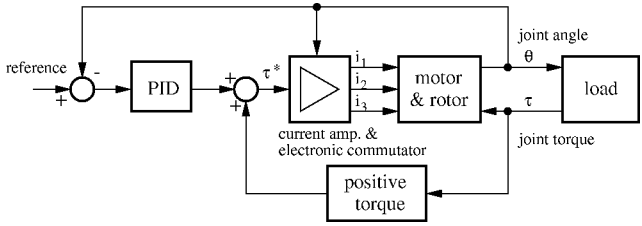

Figure 9. The control system.

is generated with minimum power dissipation. It is important to point out that the lower the dissipation, the higher the torque-to-mass ratio.

The motor winding currents are determined by modulating the torque input with the measured position, i.e.:

$$i_j = \tau^* x_j(\theta), \quad j = 1, 2, 3. \tag{3}$$

The power amplifiers work in current mode to force the current windings towards their reference values determined by the computer. The commercial torque controllers use sinusoidal commutation, i.e. sinusoidal current-angle wave shape $x_j(\theta)$, which leads to torque ripple because the distribution of magnetic flux in real electromotors is not perfectly sinusoidal.

A ripple-free commutation is developed in [6, 7]. The design requires the motor's phase torque angle and characteristics which we identify experimentally on the hydraulic dynamometer described in Section 5. An optimal Fourier coefficient of the wave form $x_j(\theta)$ that minimizes torque ripple and simultaneously minimizes copper losses is given in [6]. Another torque control strategy which also takes the effect of magnetic saturation and/or current limitations into account is given in [7]. We incorporate three separate current servo amplifiers (Advanced Motion Controls 30A20AC) to drive stator phase currents. Line isolation for the amplifier control inputs is provided by opto-couplers which also protect against ground loops. The PWM switching frequency is 22 kHz whose effect is well filtered by the inductance of the winding and inertia of the rotor.

The effectiveness of our commutation to produce ripple-free torque is demonstrated using the same dynamometer. To this end, the motor shaft is rotated by the hydraulic actuator while the motor torque is monitored by the torque transducer. A comparison of the torque ripples in the two commutations (Fig. 10) clearly shows the superior performance of our commutation.

We also demonstrate the accuracy of position tracking of our direct-drive system with and without torque ripple. To this end, in addition to the torque controller, a PID position controller, is implemented. Figure 11C and D illustrate the tracking error of the system to a ramp input set-point when the sinusoidal and the ripple-free commutations are applied separately. Figure 11 clearly shows that the tracking error reflects the torque ripple. Though the error should have been zero with respect to a

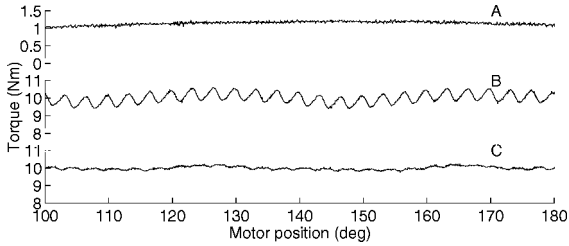

Figure 10. Joint friction torque (A), motor torque ripple with sinusoidal commutation (B) and with the ripple-free commutation (C).

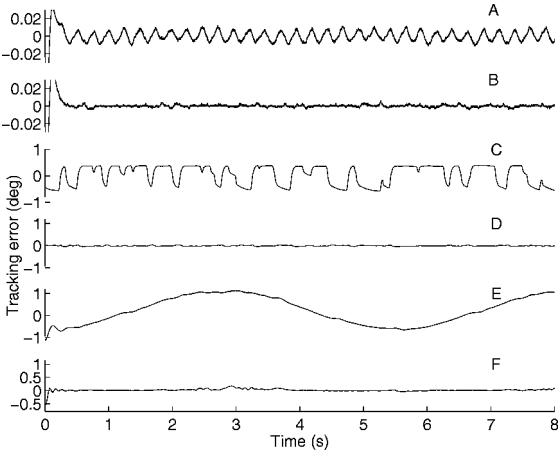

Figure 11. Position tracking error trajectories: (A) and (B) low-velocity motion with sinusoidal commutation and ripple-free commutation, (C) and (D) random torque disturbance with and without PJTF, and (E) and (F) cantilever arm with and without PJTF.

ramp input, it is oscillatory when the torque ripples exist. In the absence of actuator torque ripples, the tracking error is reduced to about the encoder resolution (0.001°).

4.2. Load torque decoupling via positive joint torque feedback (PJTF)

A high-performance motion control system requires accurate command tracking and disturbance rejection properties. Feedback systems lead to a trade-off between these requirement [17] since the disturbance cannot be attenuated without a measurement of its effect upon the system output. PJTF can be used to substantially reduce the effect of external torque disturbance or of the load torque on the motion servo system. This requires built-in torque sensing (Section 3) that is then precompensated via a feedforward loop [9–11, 18]. In this case the rotor of the direct drive motor is the plant to be controlled. The problem of finding an optimal filter for PJTF that minimizes the torque disturbance sensitivity is formulated and solved in [9]. Again, the hydraulic dynamometer is employed to evaluate the resulting disturbance rejection and load decoupling properties. In order to measure the torque disturbance sensitivity, torque disturbances are injected into the direct-drive system

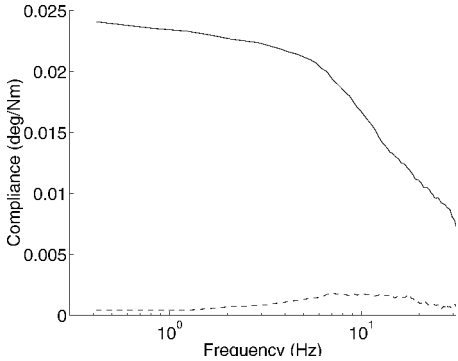

Figure 12. Torque disturbance rejection with PJTF (dashed line) and without PJTF (solid line).

Table 1.
The stiffnesses of different joint components

	Torsion stiffness (N m/rad)	Bending stiffness (N m/rad)
Motion control	4.8×10^4	—
Torque sensor	2.4×10^5	4.8×10^6
Joint bearings	—	2.5×10^7

by the hydraulic dynamometer while an arm with an adjustable payload is mounted on the motor's shaft to investigate the load decoupling properties. To this end, we command a ramp reference signal via the PID position controller while the system is exposed to the random torque disturbance produced by the hydraulic motor. Figure 11C and D illustrates the position tracking error trajectories due to the random torque disturbances without and with the torque feedback is applied. The control system exhibits relatively high disturbance sensitivity when there is no torque feedback. Figure 11 clearly shows that the tracking error is substantially reduced when the torque feedback is applied.

The disturbance attenuation is better explained in Fig. 12 (the frequency domain). As expected, at a sufficiently high frequency, the disturbance sensitivity drops due to the attenuation effect of position feedback. The optimal feedback lowers this system sensitivity remarkably over the whole frequency range.

It is worth noting that, since the actuator and position sensor are colocated, the joint angle is slightly different from the sensed angle, depending on the torsional stiffness of the torque sensor. Moreover, the bending deflection of the sensor and of the joint bearings add uncertainty in positioning accuracy. Table 1 lists the stiffnesses of different joint components, where the stiffness of the control system (recall that the torque disturbance sensitivity has compliance unit) is at the lowest.

In the next experiment, a link with a 7.2 kg mass is mounted on the motor's torque sensor. Figure 11E and F shows the tracking error of a PID position controller without and with the PJTF applied. The PID controller gains are tuned for the motor inertia to achieve a bandwidth of 10 Hz. Since the non-linear gravity torque

is not compensated, the resulting tracking error is large without the torque feedback. The same reference trajectory as in the first experiment was used in order to make a relevant comparison. Figure 11 shows the tracking error caused by the load non-linearity (sinusoidal gravity torque). The tracking error is reduced significantly when PJTF is applied.

In a summary, the control system characteristics are:

- Torque ripple $\pm 1.5\%$.
- Maximum position tracking error to a ramp input 0.003°.
- Maximum sensitivity to torque disturbance $0.0012^\circ/\mathrm{N\,m}$.

4.3. System architecture

A block diagram of the system architecture is shown in Fig. 13. The analog signals are processed by anti-aliasing filters and digitized through a multi-channel 16-bit A/D converter. Digital position data from a custom-built counter is read into the computer through a digital I/O port. The three binary current output commands are converted to analog signals via D/A converters for the inputs to the power amplifiers.

The control algorithm, written in C++, is linked to a graphical user interface (written in LabWindow) and to software drivers of the data acquisition (NI-DAQ from National Instrument). It turned out that an IBM-compatible 66 MHz 80486 computer has enough computational power to run the commutation, torque feedback and a PID position control at a high rate of 3 kHz. About 40% of this time (177 μs) is taken up by I/O, 106 μs is used for commutation, 13 μs for torque feedback and 9 μs for the PID controller.

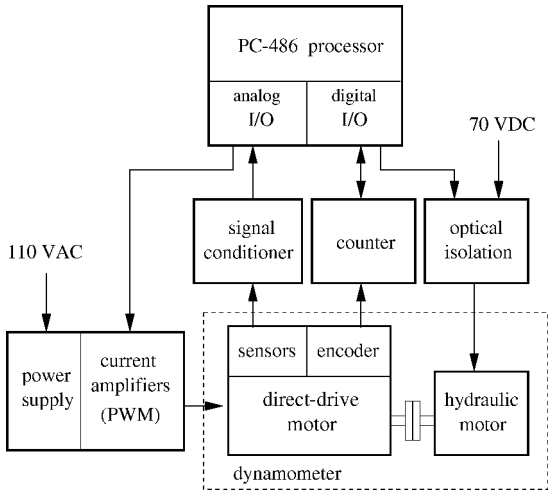

Figure 13. The system's architecture.

5. DYNAMOMETER TESTBED

The dynamometer was designed to serve several experiments. For the motor torque calibration test, the motor velocity must be regulated independent of motor torque while for the disturbance sensitivity test [9], a random torque must be generated, requiring an active load. The major design problem was the selection of an appropriate actuator for the active load. It has to be powerful enough to overcome the direct-drive motor torque, and has to operate in both velocity and torque control modes. Hydraulic actuators are well suited for this task. They are powerful and can be commanded under velocity control simply by *meter-in/meter-out* hydraulic circuits, which constrain the flow at inlet and outlet ports. The other prominent feature of the hydraulic actuator is that they cushion over the last 30° (typically) of rotation in both directions which is an ideal safety zone. A reliable shaft lock can be implemented simply by blocking the inlet and outlet ports of the hydraulic actuator. Moreover, by choosing a normally closed hydraulic valve, the system is naturally locked in the case of power failure.

Figure 14 illustrates the layout of the dynamometer. The direct-drive motor and a hydraulic rack and pinion rotary motor (Parker 113A129BME) are mounted on the rigid base of the dynamometer. The hydraulic motor's shaft is connected to that of the direct-drive motor via a reference torque transducer (Himmelstein SHC2804TC) by means of two couplings (Gam/Jakob KSS-450).

In *velocity mode*, the speed of the hydraulic motor is controlled by a pressure compensated flow control valve (meter-out circuit) which regulates the angular speed regardless of the applied direct-drive motor torque (Fig. 15). In order to cover the requirements for both low speed, 1°/s for the quasi-static test, and high speed, 1 rev/s, it is necessary to employ two different operating range flow-control valves which are brought to the hydraulic line by a manual valve. The selected flow control valves (Parker TPCS600S01 and TPCS600S6) are insensitive to variation of oil temperature and can maintain the flow (proportional to velocity) to within ±5% of the selected flow over the whole working pressure (proportional to torque). An adjustable cam and two limit switches detect the two rotational extremes and activate a solenoid valve (Parker D1VW1CJ) through a PLC unit to reverse the direction of the rotation accordingly.

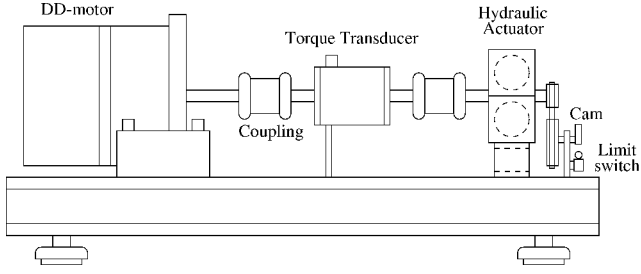

Figure 14. Schematic of the hydraulic dynamometer.

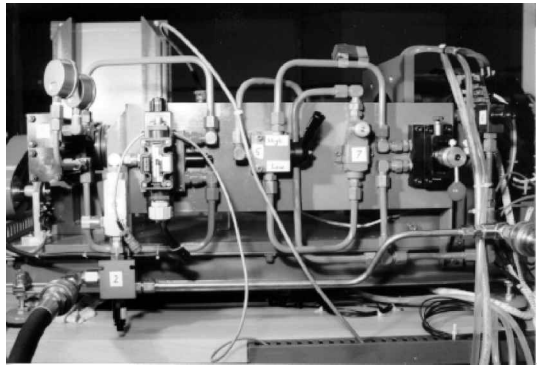

Figure 15. Hydraulic circuit of the dynamometer.

In *torque mode*, the hydraulic motor must generate pseudo-random torque disturbances and we use a solenoid directional valve to produce a time-varying torque. To this end, the valve is interfaced to the computer via a custom-built two-channel binary high-voltage isolation amplifier, permitting open loop on–off control. Suppose the hydraulic torque corresponding to the regulated hydraulic pressure is τ_{hyd}, then the hydraulic motor torque is $\{-\tau_{\text{hyd}}, 0, +\tau_{\text{hyd}}\}$ depending on how the solenoids are activated.

6. CONCLUSION

We have presented the design and control of a high-performance direct-drive system suitable for robotics and automation. The design of the mechanical and electrical components of the direct-drive system was presented. The McGill/MIT motor in a dual configuration with a housing and a special bearing arrangement was designed and built. The thermal characteristics of the motor prototype have been substantially improved by placing a cooling water tube in the proximity of the armature coil and using a thermo-conductive epoxy. The built-in torque sensor was also briefly described. The sensor's key features are its extremely high stiffness as well as insensitivity to all exogenous torque/force components that makes it suitable for joint torque sensing. A hydraulic dynamometer has been designed and constructed to work in velocity and torque control modes for calibration of the motor and for various performance tests. The overall control architecture of the joint is also briefly presented. Experimental results demonstrated that conventional sinusoidal commutation results in torque ripple, while adequate commutation almost eliminated the ripple. It is also demonstrated that a ripple-free commutation is essential for a precise tracking. The torque disturbance performance of the joint control system is evaluated when PJTF is applied. The experimental results illustrated that a significant improvement in torque disturbance rejection and load decoupling was achieved.

Acknowledgements

This project was supported in part by the PRECARN TDS Project, through MPB Technologies of Montréal, Québec.

REFERENCES

1. C. H. An, C. G. Atkeson and J. M. Hollerbach, *Model-Based Control of a Robot Manipulator.* MIT Press, Cambridge, MA (1988).
2. H. Asada and K. Youcef-Toumi, *Direct-Drive Robots.* MIT Press, London (1987).
3. J. M. Hollerbach, I. Hunter, J. Lang, S. Umans and R. Sepe, The McGill/MIT direct drive motor project, in: *Proc. IEEE Int. Conf. on Robotics and Automation*, Atlanta, GA, USA, pp. 611–617 (1993).
4. J. M. Hollerbach, I. W. Hunter and J. Ballantyne, A comparative analysis of actuator technologies for robotics, in: *The Robotics Review 2*, O. Khatib, J. Craig and T. Lozano-Perez (Eds). MIT Press, Cambridge, MA (1991).
5. R. Welburn, Ultra high torque motor system for direct drive robotics, in: *Motor Control Proc.*, pp. 17–24 (1984).
6. F. Aghili, M. Buehler and J. M. Hollerbach, Optimal commutation laws in the frequency domain for pm synchronous direct-drive motors, *IEEE Trans. Power Electron.* **15** (6), 1056–1064 (2000).
7. F. Aghili, M. Buehler and J. M. Hollerbach, Quadratic pragramming in control of brushless motors, in: *Proc. IEEE Int. Conf. on Robotics and Automation*, Seoul, pp. 1130–1135 (2001).
8. T. M. Jahns and W. L. Soong, Pulsating torque minimizing techniques for permanent-magnet ac motor drives — a review, *IEEE Trans. Ind. Electron.* **43** (2), 321–330 (1996).
9. F. Aghili, M. Buehler and J. M. Hollerbach, Motion control systems with h-infinity positive joint torque feedback, *IEEE Trans. Control Syst. Technol.* **9** (5), 685–695 (2001).
10. F. Aghili, M. Buehler and J. M. Hollerbach, Dynamics and control of direct-drive robots with positive joint torque feedback, in: *Proc. IEEE Int. Conf. on Robotics and Automation*, Albuquerque, NM, USA, pp. 1156–1161 (1997).
11. K. Kosuge, H. Takeuchi and K. Furuta, Motion control of a robot arm using joint torque sensors, *IEEE Trans. Robotics Automat.* **6** (2), 258–263 (1990).
12. F. Aghili, M. Buehler and J. M. Hollerbach, A joint torque sensor for robots, in: *Proc. ASME Int. Mechanical Engineering Congress & Exposition*, Dallas, TX, pp. 1–8 (1997).
13. MPB, Telerobotic development systems preliminary design review: Prototype 1 direct drive actuator research robot project (tds-4), Technical report, MPB Technologies, Montreal, Canada (1993).
14. R. F. George, Evaluating bearing for robots, in: *Proc. Conf. on Machine Design*, Miami Beach, FL (1983).
15. R. Sepe, McGill motor torque controller, Technical report, McGill University (1991).
16. F. Aghili, M. Buehler and J. M. Hollerbach, Sensing the torque in a robot's joint, *ASME Mech. Eng.* **120** (9), 66–69 (1998).
17. J. S. Freudenberg and D. P. Looze, Right half plane poles and zeros, and design tradeoffs in feedback systems. *IEEE Trans. Autom. Control* **30** (1985).
18. M. Hashimoto, Robot motion control based on joint torque sensing, in: *Proc. IEEE Int. Conf. on Robotics and Automation*, Scottsdale, AZ, USA, pp. 256–1261 (1989).

ABOUT THE AUTHORS

Farhad Aghili received the BSc and MSc degrees in Mechanical Engineering and Biomedical Engineering from Sharif University of Technology, Tehran, Iran, in 1998 and 1991, respectively. From 1994 to 1997, he was a Research Engineer at MPB Technologies, Montreal. In January 1998, he joined Canadian Space Agency as a contractor and is currently a Research Scientist there. His main areas of interest include robotics and automatic control.

Martin Buehler received the MEng and PhD degrees in Electrical Engineering from Yale University, New Haven, CT, in 1985 and 1990, respectively, and subsequently studied legged locomotion as a Postdoctoral Associate at the Artificial Intelligence Laboratory at MIT. In 1991, he joined the Mechanical Engineering Department at McGill University, Montreal, Canada, as a Junior Industrial Research Chair, and is currently an Associate Professor there. His main research interests are in motor control, legged locomotion, biomimetics, energetics, actuators, and robot design and control. He participates regularly in conference organization and reviews for many journals and conferences. Since 1998 he has been an Associate Editor for the *IEEE Transactions on Robotics and Automation.*

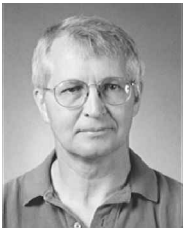

John M. Hollerbach is Professor in the School of Computing, and Adjunct Professor of Mechanical Engineering, at the University of Utah. From 1989 to 1994 he was the Natural Sciences and Engineering/Canadian Institute for Advanced Research Professor of Robotics at McGill University, jointly in the Departments of Mechanical Engineering and Biomedical Engineering. From 1982 to 1989 he was on the faculty of the Department of Brain and Cognitive Sciences and a member of the Artificial Intelligence Laboratory at MIT; from 1978 to 1982 he was a Research Scientist. He received his BS in chemistry (1968) and MS in mathematics (1969) from the University of Michigan, and SM (1975) and PhD (1978) from MIT in Computer Science. In 1984 he received an NSF Presidential Young Investigator Award, in 1988 he was named a Fellow of the Canadian Institute for Advanced Research and in 1996 he became an IEEE Fellow. He was the Program Chairman of the 1989 IEEE International Conference on Robotics and Automation, a member of the Administrative Committee of the IEEE Robotics and Automation Society from 1989 to 1993, Technical Editor of the *IEEE Transactions on Robotics and Automation* from 1989 to 1994 and Treasurer of the *IEEE/ASME Journal of Microelectromechanical Systems* from 1992 to 1997. He was a member of the 1994–1995 National Research Council Committee on Virtual Reality Research and Development. Presently he is Editor of the *International Journal of Robotics Research*, a Senior Editor of *Presence: Teleoperators and Virtual Environments* and a Governing Board member of the electronic journal *Haptics-e.* His research interests combine robotics, virtual reality and microelectromechanical systems.